

Broadband modelling along a regional shield path, Harvard recording of the Saguenay earthquake

Lian-She Zhao and Donald V. Helmberger

Seismological Laboratory, 252-21 California Institute of Technology, Pasadena, CA 91125, USA

Accepted 1990 October 29. Received 1990 September 10; in original form 1990 April 27

SUMMARY

The Saguenay earthquake, 1988 November 25, is one of the first large shield type events recorded by a broadband-high dynamic range instrument, the Streckeisen system, installed at Harvard station (HRV). The event is sufficiently large to be well recorded teleseismically and thus the source characteristics can be determined by independent means and considered known. This allows a detailed study of the propagational effects along this path, at an epicentral distance of 625 km, where the strengths of the surface waves can be compared with the crustal body phases. Broadband modelling using standard analytical techniques and flat layered models works amazingly well over the period range of 0.5–20 s. A detailed strategy for modelling broadband regional phases is given in terms of a decomposition of the vertical and radial seismograms into three segments: P_{nl} (containing P_n , pP_n , sP_n , P_mP , P coupled PL -waves); S_{nl} (containing S_n , sS_n , S_mS , etc.); and the fundamental Rayleigh waves. Information about the upper crust is obtained from the fundamental Rayleigh waves while crustal thickness and velocity gradients in the mantle are obtained from P_{nl} and S_{nl} . This particular crustal model has a thickness of 35 km with a sharp Moho and a substantial gradient in the top 20 km of the mantle, 0.01 km s^{-1} per km for both P and S velocities. The mantle velocities, $\alpha = 8.2$ and $\beta = 4.55 \text{ km s}^{-1}$ are slower than expected for a shield environment. Attenuation is not required for waveform modelling or for absolute amplitude estimation.

Key words: broadband modelling, generalized ray method (GRM), mode summation method (MSM), reflectivity.

1 INTRODUCTION

In recent years, short-period seismology has concentrated on small events and local crustal structure while long-period seismology has concentrated more on inverting source mechanisms of larger earthquakes and deep earth structure. Long-period seismograms at regional distances have not received much attention in either source studies or in studies of the Earth's shallow structure. One reason is that only small events, $4 < m < 5$, remain on scale on the standard long-period WWSSN at these distances. The source properties of these events are generally poorly understood, since they cannot be easily studied teleseismically. Thus, these events are not so useful in Earth structure investigations. Larger events produce visible P_n - and PL -waves and these waveforms have been used in earthquake studies (e.g. Helmberger & Engen 1980; Wallace & Helmberger 1982), but the surface waves of the events go off-scale. Most digital systems have, unfortun-

ately, not performed well at regional distances for assorted reasons.

With the installation of the Streckeisen seismometer and high dynamic range digitizer, the broadband nature of regional phases can now be appreciated (see Fig. 1). The HRV recording of the Saguenay earthquake, at an epicentral distance of 625 km, is one of the first such unclipped recordings of a sizable earthquake occurring in a predominantly shield region. This event is the largest earthquake to occur in over 50 years in eastern North America and was recorded both locally and teleseismically (e.g. North *et al.* 1989; Somerville *et al.* 1990). These studies provide seismic source parameters for the event (strike = 323° , dip = 65° , rake = 78° , moment = 5.0×10^{24} dyne cm, depth = 28 km), as well as some constraints on the time history.

Figure 2 gives the three-component long-period WWSSN recordings obtained by convolving the broadband data displayed in Fig. 1 with the WWSSN instrument response.

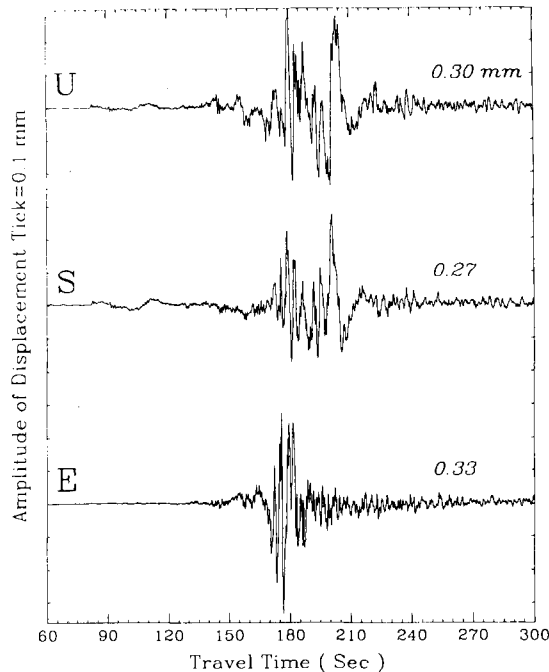


Figure 1. The broadband displacement data recorded by Harvard station (HRV) of the 1988 November 25 Saguenay earthquake. The first trace is the vertical component, where upward is positive; second trace is the radial component, positive southward; and the third trace is the tangential component, positive eastward. The numbers on the right are the maximum amplitudes in mm. The instrument response is flat in velocity between 0.0027 and 7 Hz. Integrating within this band produces the displacement records displayed.

The peak-to-peak amplitude of the Rayleigh wave is about 1.1 m. If the gain of the instrument is taken as the average WWSSN (2250), the Rayleigh wave goes off-scale on conventional records. The first 40 s of these records is controlled by the (P - SV) system. This wavetrain begins with P_n and evolves into PL and has been called P_{nl} (Helmberger & Engen 1980). The later arriving phases begin with S_n , sS_n , etc. and go off-scale somewhere near the direct S arrival. The beginning portion of this group which arrives before the fundamental Rayleigh wave will likewise be called S_{nl} for convenience.

Figure 3 displays a comparison of the broadband data and synthetics constructed from a flat-layered model. A brief comparison of these waveforms indicates that quantitative methods based on layered models work quite well, at least in a shield environment. This paper addresses some techniques and strategies which were used in deriving the above model along with numerous sensitivity studies. What can be learned from regional broadband seismograms is our main concern in this study.

2 NUMERICAL METHODS

There are many different techniques available for generating synthetics for a flat-layered model (see Aki & Richards 1980 for example). The reflectivity method (Mallick & Frazer 1988) and various modifications essentially perform a double

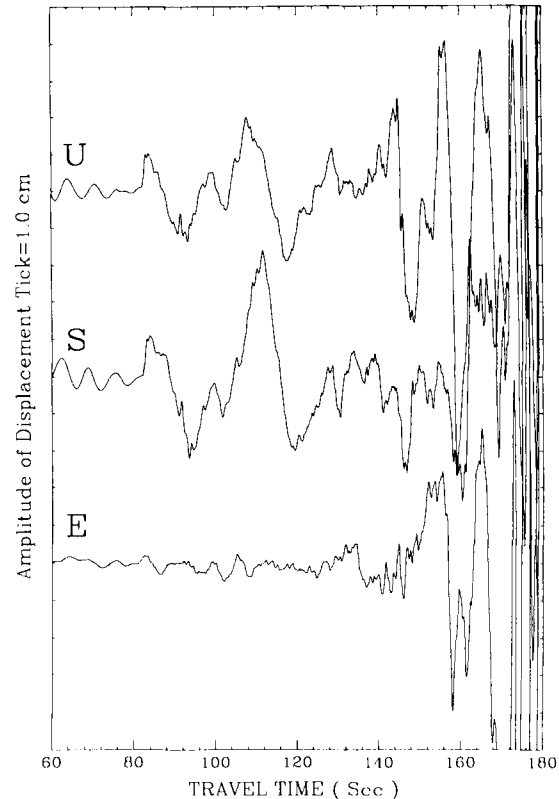


Figure 2. The broadband data convolved with the WWSSN long-period instrument response. These would be the real long-period record with a gain of 2250. The three components are the vertical, radial and tangential. The letters on the left indicate the positive directions.

integration and produce accurate results if the integration windows are properly placed with respect to the range of ray parameter and frequency. This technique lends itself to vectorization and looks more attractive than the other methods with the availability of vector computers. Comparison of synthetics generated with this approach and with generalized rays (Helmberger 1983), has been discussed by Apsel & Luco (1983) for simple models where it is possible to sum enough rays to construct the entire wavefield. The advantage of rays is that insight can be gained into the timing of individual pulses. However, in strong waveguides the number of significant multiples become large and the method becomes impractical. Fortunately, the normal mode method or mode summation method (Harkrider 1964) works well for modelling surface waves at about this time window, as we discuss next.

In this study, the earthquake will be represented by a simple point-source dislocation, which can be computed by constructing a linear combination of responses for pure strike-slip, dip-slip and 45° dip-slip sources, as discussed by Helmberger & Harkrider (1978). Synthetics of these three types of source descriptions are displayed in Figs 4 and 5, where the generalized ray results are compared with those of reflectivity and the normal mode method. The model used is the same as that considered by Apsel & Luco (1983), in their study of the various methods of generating synthetics. The bottom traces display P_n , P_mP and direct P ,

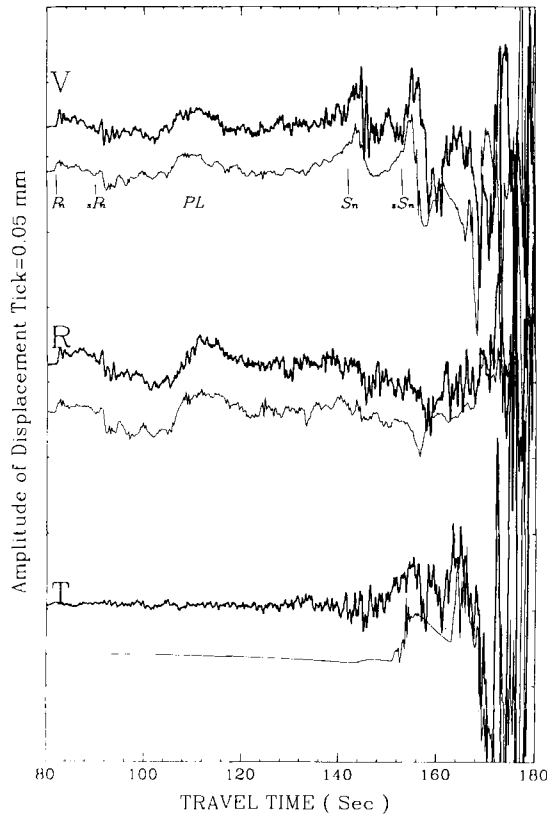


Figure 3. This figure displays the first 100 s of the broadband waveform data along with the synthetics generated by a flat-layered model found in this study. The main phases such as P_n , sP_n , and PL , S_n , and sS_n are labelled.

followed by pP_n , pP_mP and sP_n , etc. A similar set of S phases occurs near the surface waves, which appears to be included in the mode solution and produce synthetics in good agreement with the ray solution. It is difficult to prove theoretically that the direct S arrivals and multiple reflected S phases are handled properly in the modal approach because of the neglect of head waves. Although the amplitudes predicted by reflectivity and rays differ somewhat, the waveforms predicted by them are almost identical. The differences in amplitudes are caused by an assortment of analytical approximation in each individual method; however, in this particular application it appears to produce accurate enough results for our purposes. The locked mode approach (Harvey 1981) could be used to construct the entire solution but this involves considerably more computing effort. We will use all these methods in this study, exploiting the particular advantages of each as appropriate.

3 MODELLING STRATEGY

Given a stack of 10 layers with 30 parameters, we would predict a synthetic match comparable to that displayed in Fig. 3 by letting each parameter vary over 10 values. In this section we discuss a strategy of finding a good fitting model without wandering through this large parameter space. Two basic elements are necessary for this strategy to work, namely, broadband signals and the bag of seismological tools just discussed.

The strategy has four stages. First, we model a long-period version of the data assuming a single crustal layer. We find that the long-period P_n and S_n depend only on the upper mantle velocities and the average properties of the crust. Five parameters are sufficient for initial modelling, that is two velocities in the mantle, two average velocities in the crust, and crustal thickness. These parameters are easily found by mostly timing and identifying particular phases, P_n , S_n , etc. the next stage, we add some layers to the crust with the above constraint to model the fundamental Rayleigh wave.

In the third stage we model the broadband waveforms by adding some upper mantle structure, which controls the short-period signals riding on top of P_n and S_n , etc. This is achieved by assuming the single-layered crustal model and working with rays.

In the fourth stage, we compute complete synthetics using reflectivity for the layered stack and make some final adjustments by trial and error. A possible fine-tuning operation, or fifth stage, would involve a formal waveform inversion. We will not perform such an inversion here but we will show a number of parameter sensitivity studies of the models near our preferred model.

3.1 Long-period modelling

The data used in this section contain the WWSSN long-period response, and will be referred to as conventional long-period data. The beginning portion of these records are displayed at the top of the Fig. 6, essentially the P_{nl} - and S_{nl} -wavetrains. Since a layer-over-half-space model has proved effective in modelling the P_{nl} portion of these records it is natural to examine the S_{nl} portion assuming the same models and summing generalized rays. Possible models are given in Table 1 with corresponding synthetics displayed in Fig. 6. The S_n phase arriving just after 140 s, as labelled in Fig. 3, appears to be phase-shifted relative to P_n . This is the case, as is seen by examining the receiver functions describing the vertical (SZ) and radial components (SR) of motion for an incoming SV signal:

$$R_{SZ} = \frac{\eta_\alpha \eta_\beta}{\beta^2 R(p)}, \quad R_{SR} = \frac{2\eta_\beta (\eta_\beta^2 - p^2)^{1/2}}{\beta^2 R(p)},$$

where

$$\eta_\alpha = \left(\frac{1}{\alpha^2} - p^2 \right)^{1/2}, \quad \eta_\beta = \left(\frac{1}{\beta^2} - p^2 \right)^{1/2},$$

$$R(p) = (\eta_\beta^2 - p^2) + 4p^2 \eta_\alpha \eta_\beta,$$

and where α is compressional velocity, β shear velocity and p ray parameter (Helmberger 1983). For $p = 1/\beta_n$, the parameter appropriate for the S_n head wave, we obtain

$$R_{SZ} = -0.28i, \quad R_{SR} = -0.013.$$

Thus, we expect S_n and sS_n to be much stronger on the vertical component than on the radial component. Since these receiver functions are very sensitive to the station site conditions we would expect to see considerable variation in observed phase shifting from station to station.

Models 2 and 5 predict better fits to radial components, whereas models 6 and 7 do better on the vertical

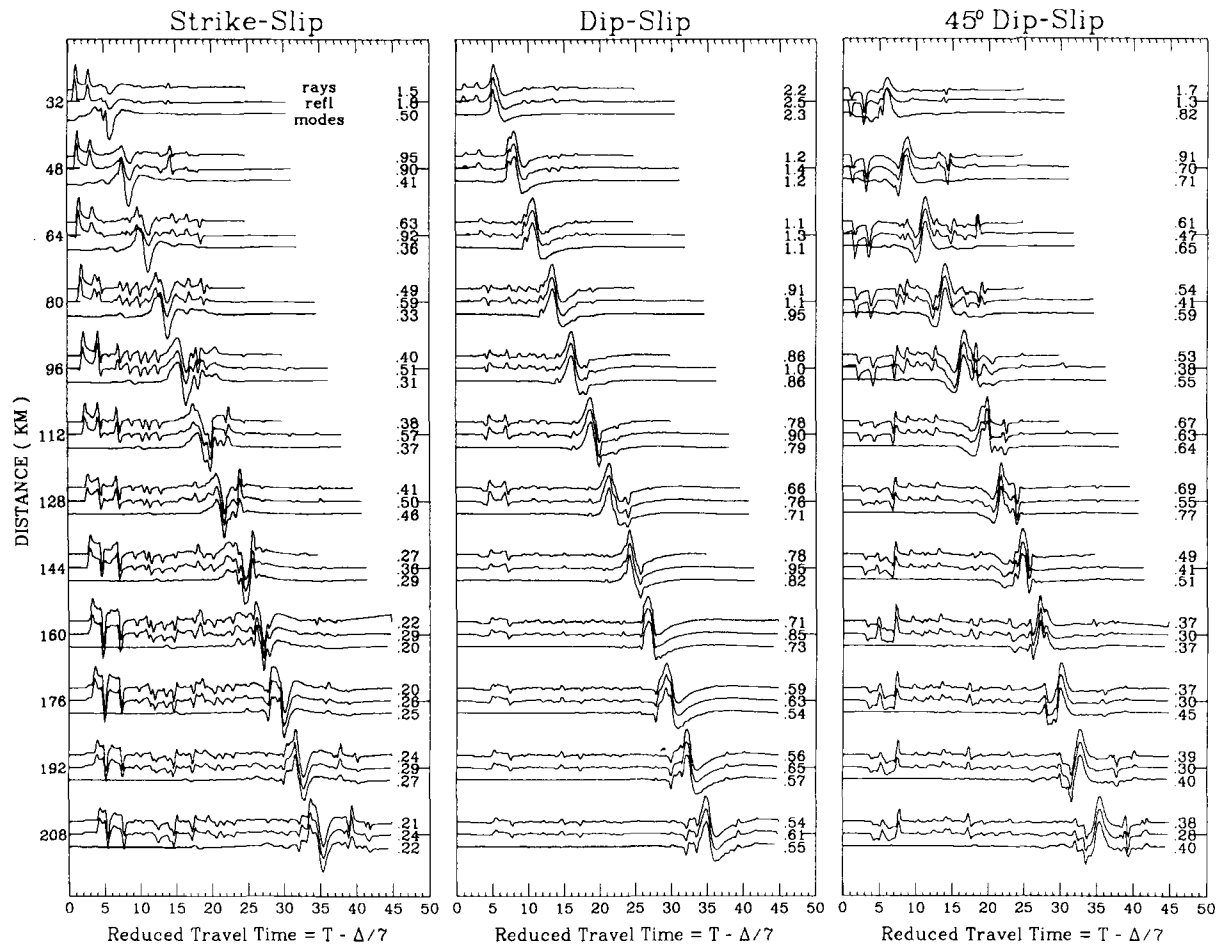


Figure 4. Comparison of the radial components of the synthetics generated by the generalized ray method (GRM), 'rays' in this figure, reflectivity, 'reft', and mode summation method (MSM), modes. The numbers on the left are the distances of the three nearest traces. The left column is for the strike-slip source; the middle for the dip-slip source; and the right for the 45° dip-slip source. The source function is a $0.2 \times 0.2 \times 0.2$ trapezoid. The moment is 10^{25} dyne cm. The source depth is 8.0 km. The numbers on the right margin of each column are the amplitudes for the corresponding traces in centimetres. The parameters of the model are: $\alpha = 6.2 \text{ km s}^{-1}$, $\beta = 3.5 \text{ km s}^{-1}$, with a 32 km thick crust; mantle velocities are $\alpha = 8.2 \text{ km s}^{-1}$, $\beta = 4.5 \text{ km s}^{-1}$. Mode synthetics include 12 modes. The parameters used for reflectivity synthetics are: decay factor 50, slowness window (0.0–0.5), frequency band (0.0025–5) Hz, $Q_\alpha(80\,000)$ and $Q_\beta(40\,000)$.

components. Since S_n is the strongest on the vertical component we chose model 7 as a preferred starting model, noting that phase shifts will be expected when we add more layers to the crust.

The best fitting model of the complete long-period seismograms, LPM, is given in Table 3 and contains five layers in the crust yielding the average crustal velocities found in Table 1, model 7. The synthetic comparison of LPM is given in Fig. 7. These synthetics were computed by summing 10 modes and assuming a 1 s triangle source function. These synthetics are aligned in absolute time except the tangential component which is shifted 4.5 s to the left, implying a slightly faster SH velocity than SV velocity. Several dozen models were investigated but this particular model explains the timing of most of the phases the best. Note that S_n (SH) is nearly nodal at HRV and, therefore, any source complexity or errors in mechanism produce strong changes in the synthetics. For this reason we have concentrated our efforts in fitting the more stable (P – SV) system where the source can be assumed known.

3.2 Broadband modelling

The source function was assumed known in the previous section but as we move to shorter periods we must be more concerned about source complexity as mentioned in the introduction. We will discuss time history sensitivity later, but in this section we have assumed an asperity type model consisting of three different trapezoids in which the δt s are (0.4, 0.05, 0.25), (0.2, 0.15, 0.15), and (0.08, 0.31, 0.23), after Somerville *et al.* (1990). The broadband synthetics displayed in Fig. 8 are appropriate for the long-period model, LPM. The overall fit is promising but lacks the shorter period signals arriving on top of S_n and sS_n . To model these we return to summing generalized rays. Fig. 9 gives the comparison of synthetics of the preferred model, short-period model, SPM (Table 3, Fig. 11), to the waveform data. The model was derived by adding some shallow mantle structure.

The shear velocity gradient at the top of the mantle has a strong effect on the S_n and sS_n behaviour as displayed in

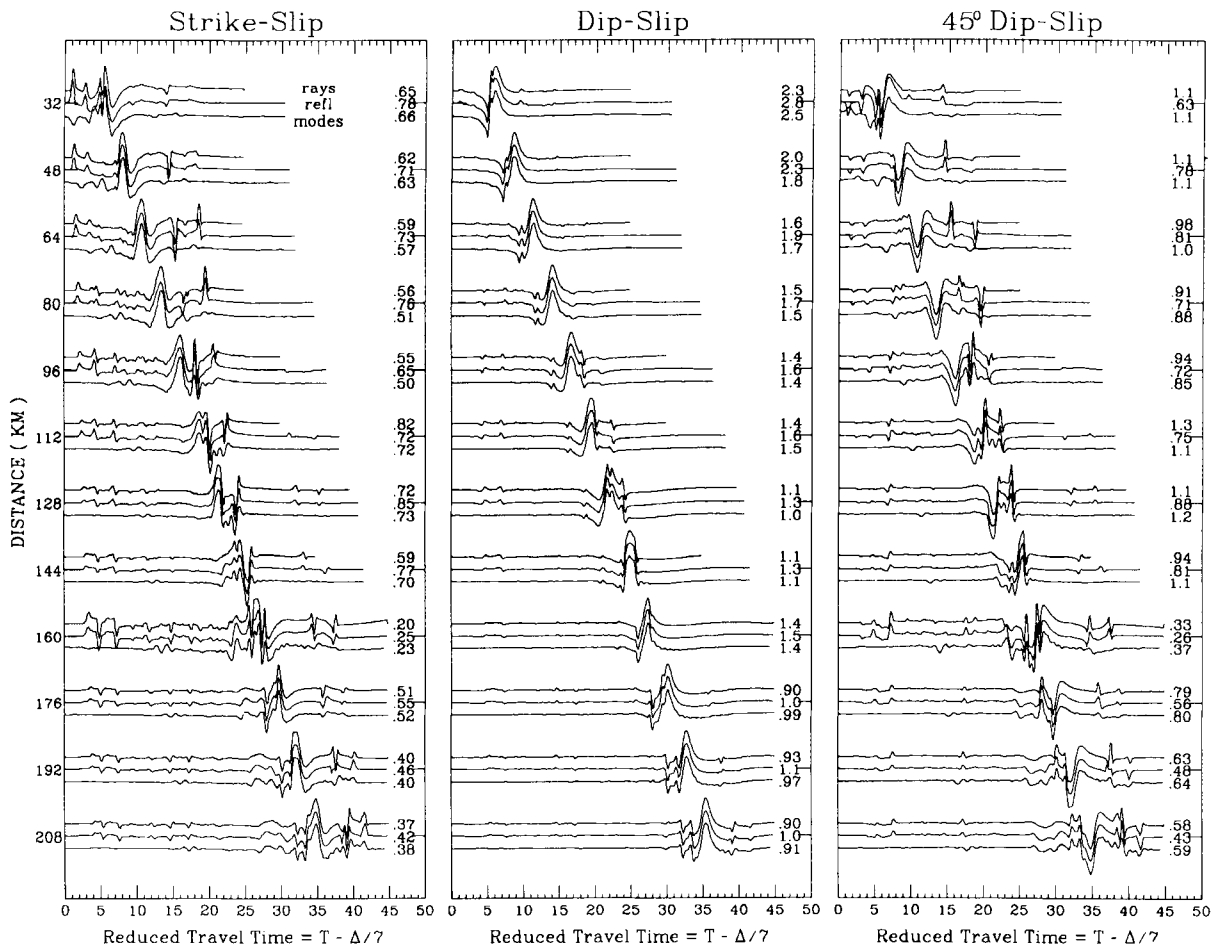


Figure 5. Comparison of the vertical components of the synthetics generated by the GRM method, reflectivity and MSM methods. The left is for the strike-slip source; the middle for the dip-slip source; and the right for the 45° dip-slip source.

Fig. 10. The models used in constructing these synthetics are given in Table 2. The blank boxes in Table 2 indicate that the layers have the same parameters as model 209. Each model is different from model 209 in one parameter, namely the shear velocity or thickness. The numbers on the left of Fig. 10 are model names. We tried dozens of models with a crustal thickness of 40 km, and concluded that the crust should be thinner to match the gradients and appearances of waveforms of S_{nl} . If we use a faster crust, model 218, see Table 2, we can see the earlier arrivals of the sP_mP group (letter a on the radial component of the synthetics of model 218, Fig. 10) and the sP_mSP_mP group (letter b), and the sS_mSS_mS group (letter c) phase, and the S_{nl} -waveform predictions are too early. Models 213 and 215 are similar to model 209 except that the thicknesses of the second layer are 20 and 5 km respectively. Model 213 predicts smaller amplitudes of S_n and sS_n phases, and discordant waveforms of sS_mSS_mS group phases. Model 215 predicts a nice fit on the radial component of the S_{nl} -wave, but the vertical component fit is not so good. The thickness of the second layer can also be estimated from the S_{nl} data. The shear velocity of third layer can be inferred from comparing the synthetics of models 209 and 211. Comparing the synthetics of the models 209 and 212, we can see that model 209 is better. We also have tried other velocities for this layer, but

4.55 km s^{-1} appears to be the best. Model 209 is the shear velocity model of the SPM, short-period model, while the compressional velocities are obtained by modelling the broadband P_n data described below.

A similar sensitivity study of the P_{nl} -waveform was applied and used to adjust the P velocity gradient while holding the shear velocity structure fixed. The best fitting short-period model, SPM, found in this fashion is given in Table 3. Note that the lower portion of this model can not be resolved by this data and therefore we have simply adopted a model extended at constant compressional and shear velocities. The appearance of S_n synthetic waveforms of the mode summation method suggests that this constant velocity layer may not have a shear velocity as high as 4.775 km s^{-1} in a layer of thickness of at least 90 km.

3.3 Fine tuning

In order to fit the surface waves better, we combine the long-period model and the short-period model and arrive at the best model, MPM (see Fig. 11 and Table 3). At this step, we fix the gradient at the top of the mantle and make some adjustments in the five-layered crustal model discussed earlier. The normal mode method was applied here since

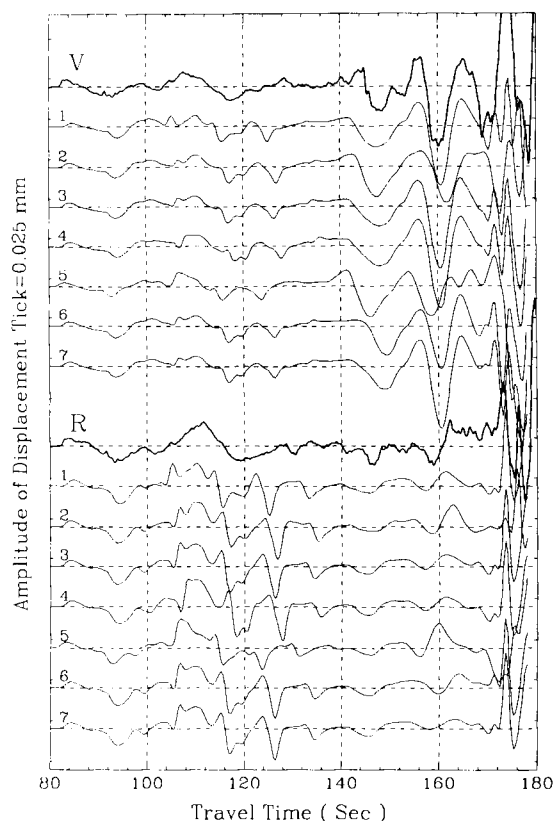


Figure 6. Comparison of the long-period P_{ni} and S_{ni} data and the synthetics generated for different models. The upper group of traces are vertical components, the lower are radial components. The models used are given in Table 1. The numbers on the left are the model numbers. The source function is a triangle (1, 0, 1).

the fundamental Rayleigh waveform is sensitive to the crustal velocity gradient.

Figure 12 displays the long-period data along with the synthetics of three models, LPM, MPM, and SPM. The second, third and fourth traces of each group are the synthetics of model MPM, SPM and LPM respectively. Models LPM and MPM predict a reasonable fit to the fundamental Rayleigh waveforms, and models SPM and MPM predict a good fit to the early portion of S_{ni} waveforms.

As a final check, we used the reflectivity method to construct synthetics for the model MPM. The synthetic comparisons are given in Fig. 13. The first 100 s of the synthetics fit the data well. In this calculation, we used a

Table 1. Models for P_{ni} -waves.

Model	1	2	3	4	5	6	7
α	6.50	6.40	6.40	6.30	6.40	6.40	6.40
β	3.70	3.65	3.70	3.70	3.65	3.70	3.70
Thick	40.0	40.0	40.0	40.0	35.0	40.0	40.0
α	8.10	8.20	8.20	8.20	8.20	8.20	8.20
β	4.70	4.70	4.70	4.70	4.70	4.65	4.68
Thick							

α is compressional velocity, β is shear velocity.

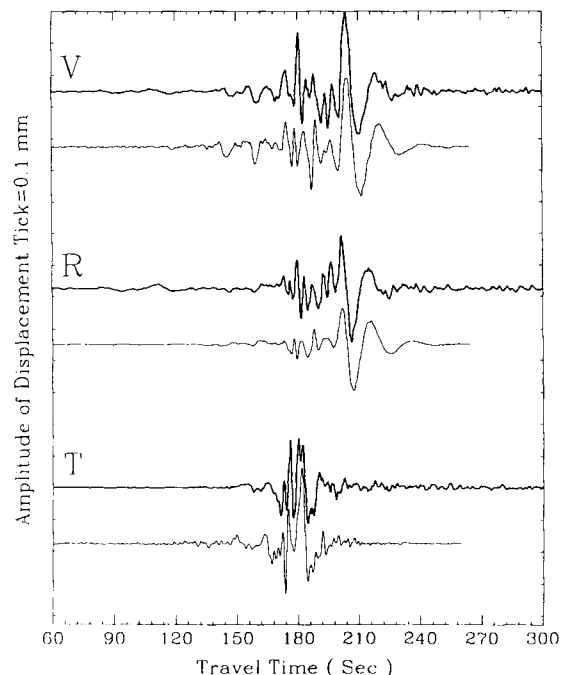


Figure 7. Comparison of the synthetics of the long-period model, LPM, and the long-period data. 10 modes were used in constructing synthetics for model LPM. The tangential component of the synthetics has been shifted to the left by 4.5 s. The upper traces are the observed waveforms. The observations and synthetics are on the same scale.

slowness window of 0.0–0.4 and a frequency band 0.004–4 Hz, assuming an exponential decay factor of 50 ($Q_\alpha = 8600$ and $Q_\beta = 6200$).

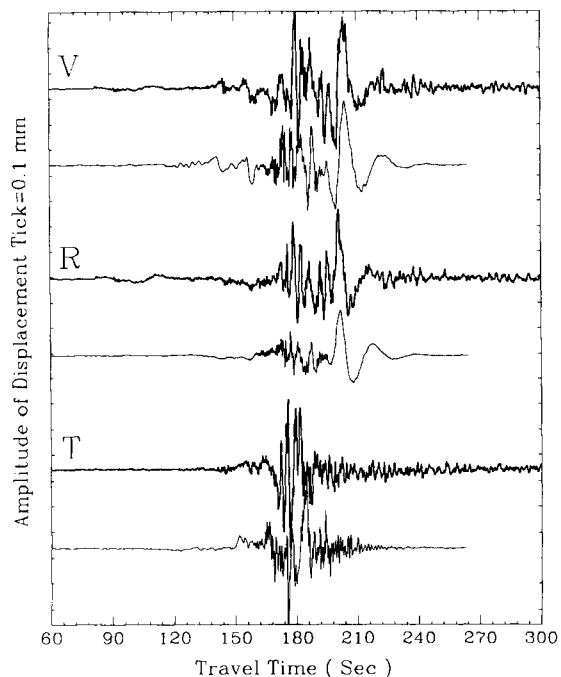


Figure 8. Comparison of the broadband data and the synthetics of the long-period model, LPM. Eight modes were used to make these synthetics. The tangential component of the synthetics has been shifted to the left by 1.5 s.

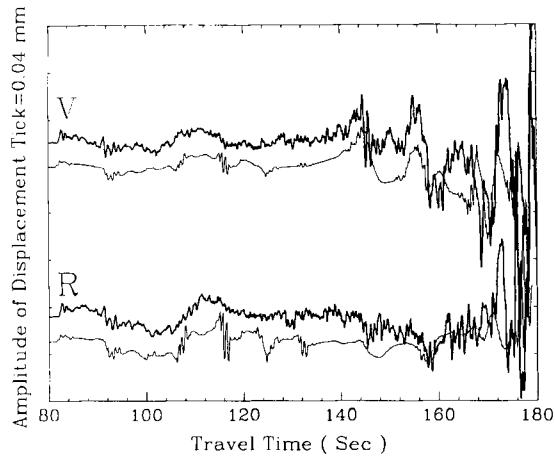


Figure 9. Comparison of the broadband data and the synthetics of the final short-period model, SPM. The synthetics were generated with the GRM.

4 SOURCE EFFECTS

So far, we have assumed that the earthquake source parameters were well determined by other studies, namely that the strike, dip and rake angles are roughly 323° , 65° and 78° respectively. The source depth was estimated by regional P_{nl} and teleseismic depth phases to be near 28 km (Somerville *et al.* 1990; North *et al.* 1989). The source time

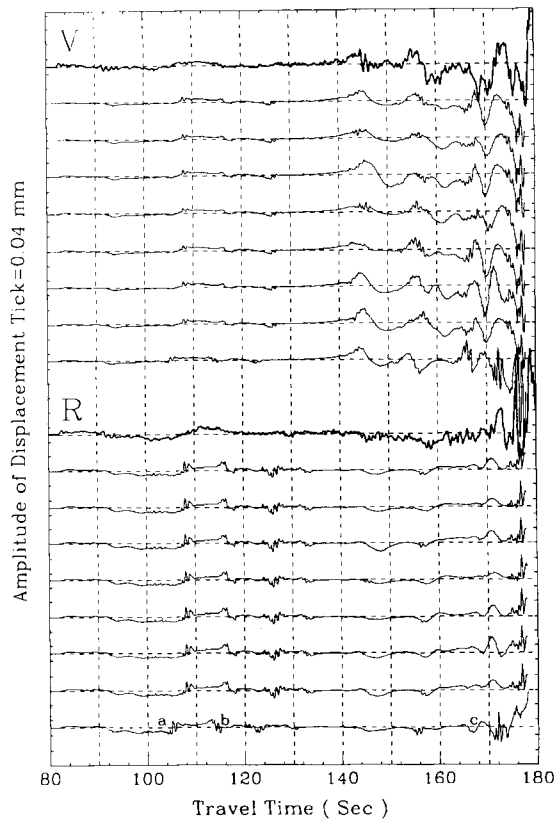


Figure 10. Sensitivity study of the waveforms of S_{nl} - and P_{nl} -waves to model parameters. The numbers on the left are model numbers indicated in Table 2. The letters a, b, and c on the bottom radial component of the synthetics indicate sP_mP , sP_mSP_mP , and sS_mSS_mS groups of phases respectively.

Table 2. Models for sensitivity study of P_{nl} - S_{nl} (Fig. 10).

MODEL	209	211	212	213	214	215	216	218
α	6.23							6.4
β	3.6							3.7
thickness (km)	35.0							35.0
α	8.06			8.06		8.06		
β	4.6			4.6		4.6		
thickness (km)	10.0			20.0		5.0		
α	8.2	8.2			8.2		8.2	
β	4.7	4.65			4.7		4.7	
thickness (km)	10.0	10.0			20.0		5.0	
α	7.97		7.8					
β	4.55		4.45					
thickness (km)								

Table 3. Model comparison; SPM, LPM, and MPM.

LPM			SPM			MPM		
α	β	Th	α	β	Th	α	β	Th
5.97	3.44	8.0				6.04	3.49	8.0
6.18	3.57	8.0				6.24	3.61	8.0
6.36	3.68	8.0	6.30	3.60	35.0	6.30	3.70	8.0
6.52	3.77	8.0				6.52	3.77	8.0
6.57	3.80	8.0				6.58	3.80	3.0
			7.90	4.60	10.0	7.90	4.60	10.0
8.20	4.68	40.0	8.10	4.70	10.0	8.10	4.70	10.0
8.36	4.775	65.0	8.20	4.55	90.0	8.20	4.55	90.0
8.27	4.723	35.0	8.27	4.723	35.0	8.27	4.723	35.0
8.13	4.64	45.0	8.13	4.64	45.0	8.13	4.64	45.0

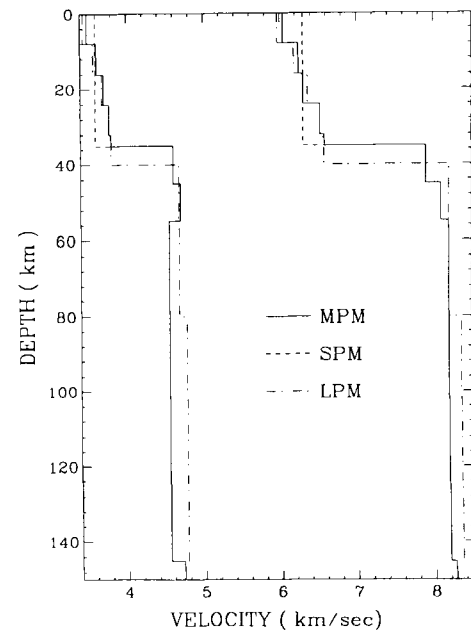


Figure 11. The upper 150 km of the models: long-period model, LPM; short-period model, SPM and final model, MPM. The bottom portion of SPM is the same as that of MPM.

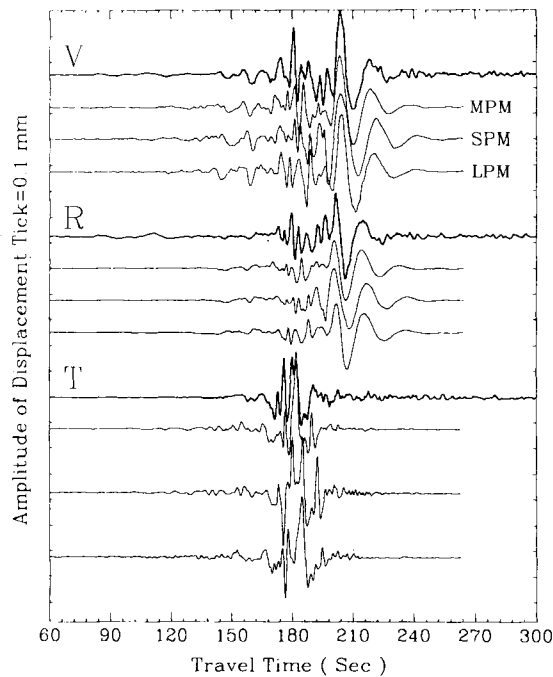


Figure 12. Comparison of the synthetics of the different models with the long-period data. The top traces are observed; the second is the synthetics of the final model, MPM; the third is that of the short-period model, SPM; and the fourth is that of the long-period model, LPM. A 1.5 s time shift to the left was applied to all the tangential components of the synthetics.

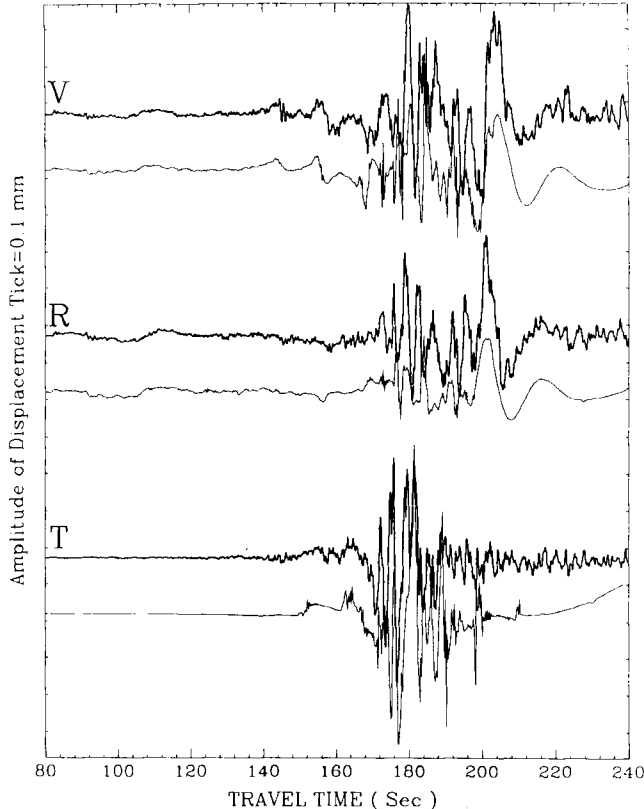


Figure 13. Comparison of the whole broadband data with the synthetics of model MPM. The synthetics were generated using the reflectivity method. The tangential component of the synthetic was shifted 1.5 s to the left.

history is not so well known nor are the rupture properties. The latter become important for regional phases, especially at short periods.

In this section, we will discuss what can be inferred from these single station regional broadband records if we know the velocity structure of the path. Assuming that our velocity model is correct, we now perturb the above source parameters and test the sensitivity of the broadband waveforms. Because of the amplitude difference between the weak P_{nl} -waves relative to the surface waves, we have displayed these sensitivity results in two sections, namely P_{nl} and S_{nl} together and a separate scale for the larger S_{nl} and surface waves.

In Fig. 14 we display the sensitivity of the strike, dip and rake angles, while holding the other two parameters fixed at the original values. Varying the strike appears to change the overall amplitude and the ratio without affecting the ratio of P_{nl} to S_{nl} . The ratio of P_n to PL drops somewhat for strikes less than 323° and does not match the observation as well. A similar feature occurs when the dip angle falls below 55° . The original dip looks the best. Varying the rake produces the most interesting results where we see a change in the sS_n -waveshape, becoming sharper for pure thrust angles. The radial synthetics for the $\lambda = 88^\circ$ looks the best, as determined by overlay, whereas the vertical fits $\lambda = 78^\circ$ are slightly better in terms of P_{nl} - S_{nl} amplitude ratio.

Figure 15 displays the long-period WWSSN data along with the synthetics of different source mechanisms. The source mechanisms do not have much effect on the surface waveforms, but do affect the amplitudes. A smaller rake or a smaller dip appears to fit the Love waveform data better than the original orientation. Note that S (SH) is near a node and, thus, is susceptible to non-planar fault effects. Since this event is known to contain at least two strong asperities it is possible that they have slightly different orientations and this could cause the above discordant behaviour. One of the reasons for concentrating on the P - SV system is the insensitivity to source descriptions relative to the unknown details needed to study SH as mentioned earlier.

Figure 16 shows the source depth effects on the P_{nl} - and S_{nl} -waveforms. The absolute traveltimes of P_n decreases with the depth as expected, as well as the time separation between P_n and sP_n . The S_{nl} -wavetrain does not seem to change shape as much as one might have expected. The source depth should be not difficult to determine if the waveforms of the P_{nl} - and S_{nl} -waves are used for a well-calibrated path. The synthetics for a depth of 28 km fit the data the best, which should be of no surprise. Clearly, the depth constraint is the most important of all the assumptions about source properties with respect to modelling. We could have easily adjusted the crustal thickness or velocities to compensate sP_n times, etc.

Source time history sensitivity is displayed in Fig. 17 where various possible time histories are given on the right. These time histories originate from different data sets from this event, and are all idealizations of complicated phenomena. The simplest ones were derived from modelling teleseismic short- and long-period P -waves as discussed earlier, namely (b) and (c). Case (b) was used in the long-period modelling where one usually uses a relatively coarse time sampling and thus a simple triangle is sufficient.

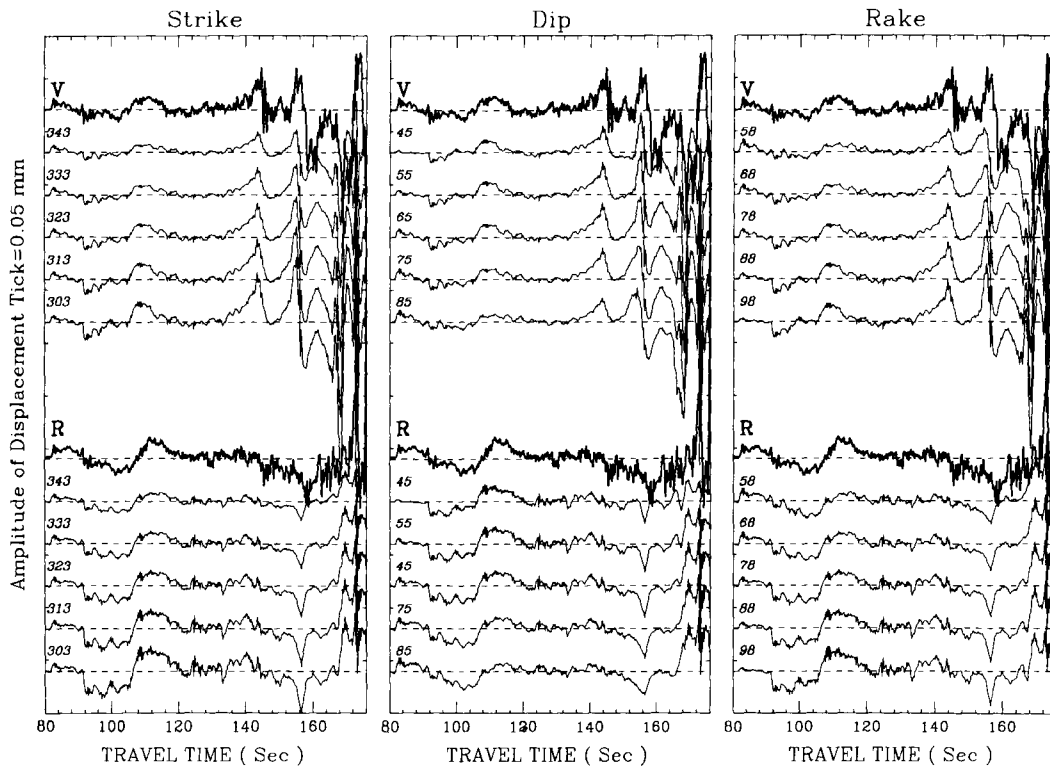


Figure 14. Sensitivity analysis of waveform changes do to variations in strike with $\delta = 65^\circ$, $\lambda = 78^\circ$ fixed, left column; in dip with $\theta = 323^\circ$, $\lambda = 78^\circ$ fixed, middle column; and in rake with $\theta = 323^\circ$, $\delta = 65^\circ$ fixed, right column. The Green's functions used here are the same as those in Figs 3 and 13.

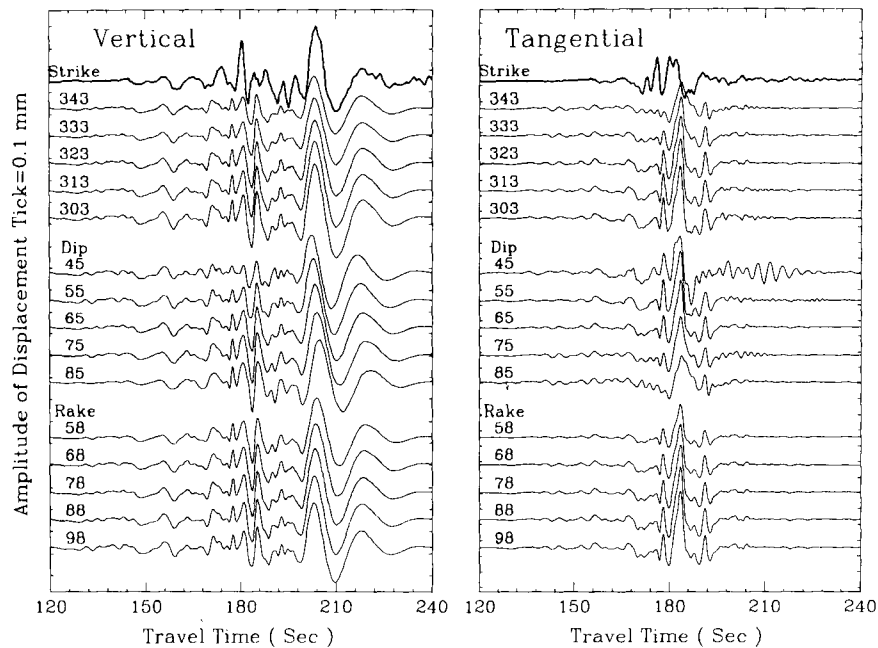


Figure 15. Sensitivity study of surface waveform data and amplitude to variations in strike, dip and rake. The MSM technique was used to generate these synthetics. The vertical components are given on the left and the tangential components on the right holding the other parameters fixed as in Fig. 14.

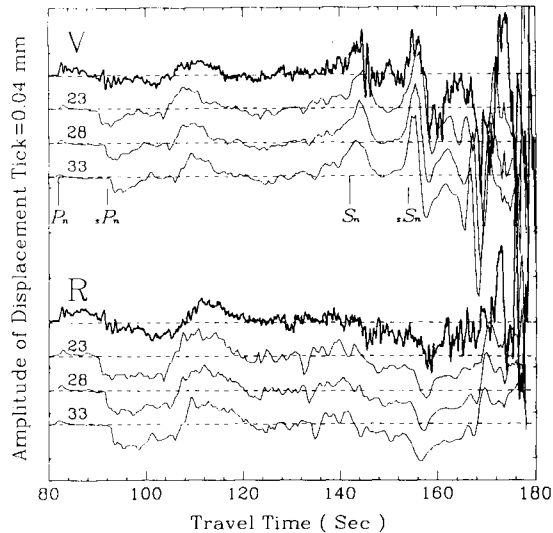


Figure 16. Source depth sensitivity analysis where the upper four traces display the vertical components, and the lower traces display the radial components. The first trace of each set is the broadband data followed by synthetics for various depths.

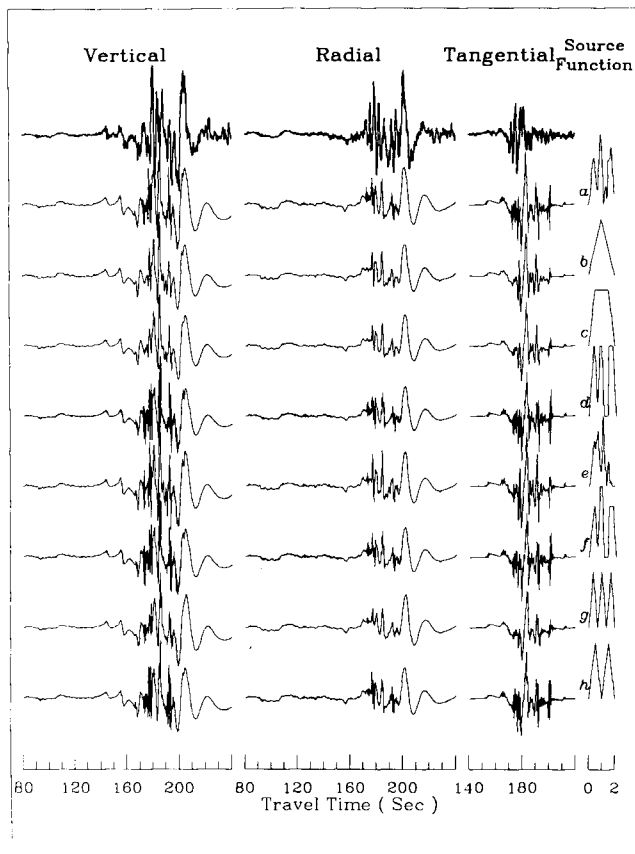


Figure 17. Sensitivity analysis of the waveform effects do to variations in source history. The left column shows the vertical components of the data and synthetics. The middle two show radial and tangential components. The column on the right indicates the various source histories used with the corresponding synthetics on the left. These are reflectivity synthetics.

The more detailed information about source complexity comes from the strong motion data. Far-field approximations of the time histories depend on direction with two possible sources (a) and (e) proposed by Somerville & Helmberger (1990) with case (e) preferred. Case (d) was used in the broadband modelling discussed earlier which is an analytical approximation to case (a) (Somerville *et al.* 1990). Cases (f), (g) and (h) are still more approximations. An overlay comparison of source function (e) with the data appears to be the best although there is not very much difference between the synthetics.

The point of this section was not necessarily to help constrain this particular earthquake but to display the source resolving power once these Green's functions are established. This model and associated Green's functions can be used to study other events roughly along this path such as older historic events recorded at Weston, etc.

5 DISCUSSIONS AND CONCLUSIONS

Our velocity structure along the path from Quebec to Harvard is distinctly slower than proposed in other studies. For example, the shear velocity of the lid of the model, $4.6\text{--}4.7\text{ km s}^{-1}$, is slower than that of either the ATL model, 4.75 km s^{-1} (Grand & Helmberger 1984a), or the SNA model, 4.8 km s^{-1} (Grand & Helmberger 1984b). In a tomographic inversion study for shear velocity beneath the North American Plate, Grand (1987) concluded that the upper 140 km of the crust and mantle of this region was very fast although he did find a major velocity boundary along this path at greater depths. It seems that the data we used do not agree with this fast structure. Perhaps S-wave splitting is occurring with the SH velocity exceeding the SV velocity by about 3 per cent. This would be compatible with the results of Gee & Jordan (1989) for the Siberian plateau. Another explanation may arise from epicentral distance uncertainty, since the velocities are sensitive to the distance and origin time. For example, if the epicentral distance were 640 km instead of 625 km, the model would be 2 per cent slower than the SNA model (Fig. 18 and Table 4). Note that

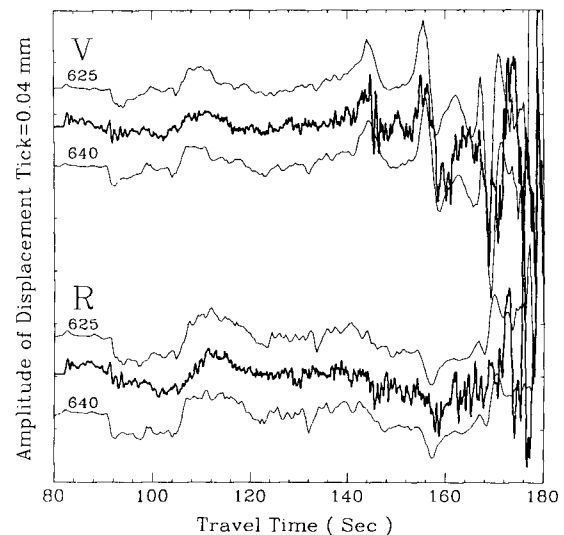


Figure 18. Comparison of the synthetics generated from model MPM, and the model for 640 km (Table 4) with the broadband data displayed in the middle trace of each set.

Table 4. Model comparison.

625 km			640 km		
α	β	Th	α	β	Th
6.04	3.49	8.0	6.26	3.56	8.0
6.24	3.61	8.0	6.45	3.67	8.0
6.30	3.70	8.0	6.59	3.75	8.0
6.52	3.77	8.0	6.71	3.82	8.0
6.58	3.80	3.0	6.71	3.82	3.0
7.90	4.60	10.0	8.10	4.70	10.0
8.10	4.70	10.0	8.35	4.80	10.0
8.20	4.55	90.0	8.40	4.65	90.0

waveform fits are comparable to those found earlier. Errors in distances up to 15 km or more are possible, if the location is determined by teleseismic means. For instance, the distance between the location given by USGS and that given by HRV is 12 km for this event. However, in this particular case, the location, based on close-in aftershock data recorded by the Geological Survey of Canada (North *et al.* 1989) is probably accurate to 5 km. Finally, perhaps this path to Harvard, which runs along an old suture zone, is indeed slow and this slowness is caused by a regional anomaly (Sykes 1978).

The Q_β estimates of eastern North America are of order 300 for the crust, and less than 200 for the mantle (Hwang & Mitchell 1987). Synthetics generated with these values do not match the data as well as those generated with $Q_\beta = 6200$, $Q_\alpha = 8600$ do, which we assumed to simulate the infinite Q case. However, these Q values were derived for periods greater than 50 s and are probably not appropriate to these broadband records. In any case, the observations have more high frequencies than the synthetics at large Q 's and lowering Q does not look promising, at least for this particular path.

In summary, we presented a strategy for modelling broadband records at regional distances. The basic procedure consists of breaking the seismograms into segments where the waveforms of each segment prove sensitive to a particular portion of the waveguide. Three divisions appear to be the most useful, namely, (a) the P_{nt} segment containing P_n , pP_n , sP_n , P_mP , its multiples and P -coupled PL ; (b) the S_{nt} segment containing S_n , sS_n , S_mS , its multiples and S -coupled PL ; and (c) the fundamental Rayleigh wave segment.

(a) P_{nt} -wavetrain

The long-period component of the P_{nt} -wavetrain is controlled by the crustal thickness, the average crustal velocities, and the compressional velocity of the mantle. Its shorter period contributions are influenced by the sharpness of the Moho transition, the fine structure at the top of the mantle, compressional velocity gradients, etc.

(b) S_{nt} -wavetrain

This segment is probably the most difficult to appreciate. It has been studied less, and produces the strongest short-period arrivals, usually called the L_g phase. The

beginning portion of this wavetrain consists of S_n , and sS_n , as identified in this study, and can be used to study the shear velocity properties of the top of the mantle. Further into this wavetrain, one finds stronger arrivals associated with multiple-bounce S_mS and probably S -coupled PL from the uppermost surface layer. These phases are included in the synthetics of both methods, the normal mode method and reflectivity, but have not been subdivided into individual ray groups for special study. The longer period S -coupled PL -waves trapped in the crustal layer over a mantle waveguide have been studied extensively, and are responsible for contaminating teleseismic SV body waves to the extent that they are rarely used in source studies. The laterally varying surface waveguide consisting of the upper few kilometres of the Earth is likely to produce similar types of semi-trapped shorter period P -waves. Such waves are easily identified in local records (Dreger & Helmberger 1990), but have not been investigated at these ranges.

(c) Fundamental Rayleigh wavetrain

The fundamental Rayleigh waves are controlled by the shear velocity structure of the crust at these ranges and are not particularly sensitive to the mantle parameters. This statement is generally true for the fundamental Love waves as well (Zhao, Helmberger & Harkrider, 1991). Normal surface wave modes are easily generated for possible models and fitting this portion of the record proved relatively easy.

In conclusion, this study demonstrates that broadband regional phases can be modelled. This study, thus, has several implications with respect to source discrimination and with respect to exploration of the lithosphere. Earlier studies have established the ease of modelling the beginning portion of a long-period record in terms of P_n , pP_n , and sP_n ; i.e. a layer over half-space. Apparently, the S_n , pS_n , and sS_n window is also easily modelled on the vertical component. The phases can be seen at low magnitudes where teleseismic signals are no longer recorded above the noise. For example, the Saguenay earthquake produced only a few high-quality teleseismic waveforms. Thus, S_{nt} and P_{nt} on standard long-period WWSSN records can probably be used to study events down to magnitude 4.5 since P_{nt} 's have proved useful down to magnitude 5 and S_{nt} 's are considerably stronger. In addition, the strongest short-period signals are related in timing with the long-period arrivals. One can use the latter as a guide in constructing broadband models (many layers) and scattering models for still shorter periods.

Presently, it has proven quite difficult to discriminate small explosions from small earthquakes as well as the $m_b:M_s$ ratio does at larger magnitudes (see Taylor *et al.* 1989). One excellent method of establishing the identification of an event is by depth and, therefore, by depth phases. Calibrating crustal models and the development of regional Green's functions addresses this problem.

Exploration of the continental lithosphere in interesting regions has proven difficult. Molnar (1989) and his colleagues have spent a great deal of effort studying the collision zone between the Indian and Asian plates. The absolute velocities of P and S at the top of the mantle is one of the key factors in establishing temperatures there. Furthermore, velocity gradients can probably establish

whether heating is taking place from the top-down or vice versa (Zhao *et al.* 1991). Thus, broadband modelling of regional data from southern platforms of the Soviet Union and transition zones of western China can provide some key information and will be presented in future reports.

ACKNOWLEDGMENTS

We would like to thank David G. Harkrider, Mrinal Sen, Laura Jones, Bradley Woods, Larry Burdick and Hiroo Kanamori for their help with the computer codes and their reviews. We would like to thank Adam Dziewonski for setting up this excellent recording system. We would also like to thank Paul Spudich, George Choy and several official reviewers for their comments. This research was supported by the National Science Foundation grant EAR-89-04767 and by the Advanced Research Projects Agency of the Department of Defense and was monitored by the Air Force Geophysical Laboratory under the contract F1962889K0028. Contribution No. 4839, Division of Geological and Planetary Sciences, California Institute of Technology, Pasadena, California.

REFERENCES

- Aki, K. & Richards, P. G., 1980. *Quantitative Seismology, Theory and Methods*, W. H. Freeman and Co., San Francisco.
- Apsel, R. J. & Luco, J. E., 1983. On the green's functions for a layered halfspace, *Bull. seism. Soc. Am.*, **73**, 931–952.
- Dreger, D. & Helmberger, D. V., 1990. Broad-band modeling of local earthquakes, *Bull. seism. Soc. Am.*, **80**, 1162–1179.
- Gee, L. S. & Jordan, T. H., 1989. Polarization anisotropy and fine-scale structure of the Eurasian upper mantle, *Geophys. Res. Lett.*, **8**, 824–827.
- Grand, S. P., 1987. Tomographic inversion for shear velocity beneath the North American plate, *J. geophys. Res.*, **92**, 14 065–14 090.
- Grand, S. P. & Helmberger, D. V., 1984a. Upper mantle shear structure beneath the northwest Atlantic Ocean, *J. geophys. Res.*, **89**, 11 465–11 475.
- Grand, S. P. & Helmberger, D. V., 1984b. Upper mantle shear structure of North America, *Geophys. J. R. astr. Soc.*, **76**, 399–438.
- Harkrider, D. G., 1964. Surface waves in multilayered elastic media, I. Rayleigh and Love waves from buried sources in a multilayered elastic half-space, *Bull. seism. Soc. Am.*, **54**, 627–679.
- Harvey, D., 1981. Seismogram synthesis using normal mode superposition: The locked mode approximation, *Geophys. J. R. astr. Soc.*, **66**, 37–61.
- Helmberger, D. V., 1983. Theory and application of synthetic seismograms, in *Proceedings of the International School of Physics (Enrico Fermi), Course LXXXV, Earthquakes: Observation, Theory and Interpretation*, pp. 174–222, eds Kanamori, H. & Boschi, E., North-Holland.
- Helmberger, D. V. & Engen, G. R., 1980. Modeling the long-period body waves from shallow earthquakes at regional distances, *Bull. seism. Soc. Am.*, **70**, 1699–1714.
- Helmberger, D. V. & Harkrider, D. G., 1978. Modeling earthquakes with generalized ray theory, in *Proceedings of IUTAM Symposium: Modern Problems in Elastic Wave Propagation*, pp. 499–517, eds Miklowitz, J. & Achenback, J., Wiley, New York.
- Hwang, H.-J. & Mitchell, B. J., 1987. Shear velocities, Q_β , and the frequency dependent of Q_β in stable and tectonically active regions from surface wave observations, *Geophys. J. R. astr. Soc.*, **90**, 575–613.
- Mallick, S. & Frazer, L. N., 1988. Rapid computation of multioffset vertical seismic profile synthetic seismograms for layered media, *Geophysics*, **55**, 479–491.
- Molnar, P., 1989. The geologic evolution of the Tibetan Plateau, *Am. Scientist*, **77**, 350–360.
- North, R. G., Wetmiller, R. J., Adams, J., Anglin, F. M., Hasegawa, H. S., Lamontagne, M., Du Berger R., Seeber, L. & Armbruster, J., 1989. Preliminary results from the November 25, 1988 Saguenay (Quebec) earthquake, *Seism. Res. Lett.*, **60**, 89–93.
- Somerville, P. G. & Helmberger, D. V., 1990. The effect of crustal structure on the attenuation of strong ground motion in eastern north America, *Fourth US National Conference of Earthquake Engineering at Palm Springs*, May 1990, submitted.
- Somerville, P. G., McLaren, J. P., Saikia, C. K. & Helmberger, D. V., 1990. The November 25, 1988 Saguenay, Quebec earthquake, *Bull. seism. Soc. Am.*, **80**, 1118–1143.
- Sykes, L. R., 1978. Intraplate seismicity, reactivation of preexisting zones of weakness, alkaline magmatism, and other tectonism postdating continental fragmentation, *Rev. Geophys. Space Phys.*, **16**, 621–688.
- Taylor, S. R., Denny, M. K., Vergino, E. S. & Glaser, R. E., 1989. Regional discrimination between NTS explosions and western U.S. earthquakes, *Bull. seism. Soc. Am.*, **79**, 1142–1172.
- Wallace, T. C. & Helmberger, D. V., 1982. Determining source parameters of moderate-size earthquakes from regional waveforms, *Phys. Earth planet. Inter.*, **30**, 185–196.
- Zhao, L.-S., Helmberger, D. V. & Harkrider, D. G., 1991. Shear-velocity structure of the crust and upper mantle beneath Tibetan and Southeastern China, *Geophys. J. Int.*, in press.